scientific reports

Check for updates

OPEN

Ligand modulated charge transfers in Z-scheme configured Ni-MOF/g-C$_3$N$_4$ nanocomposites for photocatalytic remediation of dye-polluted water

Gayathri Karthik, Sakar Mohan$^{\boxtimes}$ & R. Geetha Balakrishna$^{\boxtimes}$

The development of photocatalysts must be meticulous, especially when they are designed to degrade hazardous dyes that cause mutagenesis and carcinogenesis. In this meticulous approach, Ni-based metal–organic frameworks with different ligands, including terephthalic acid (NTP), 2-aminoterephthalic acid (NATP), and their composite with g-C$_3$N$_4$ (NTP/GCN, and NATP/GCN) have been synthesized using hydrothermal method. Structural analysis by XRD and ATR-IR revealed synergistic properties due to robust chemical interactions between the NATP-MOFs and GCN systems. A flower-like morphology was observed for both NTP and NATP, while their composites showed mixed-particulate structures mimicking the morphology of GCN. Optical analyses indicated visible-light driven properties with modulated recombination resistance in the system. Among the synthesized bare and composite systems, NATP/GCN exhibited the highest photocatalytic degradation efficiency for the cationic rhodamine B dye (~ 93% in 120 min), while it was relatively less efficient for the anionic Congo red dye, (~ 64% in 120 min). The insights gained from the fundamental characterizations including Mott–Schottky, scavenger, and electrochemical impedance analysis revealed that the amino-groups in NATP/GCN composite offered the band edge potentials suitable for the effective generation of energetic radical species with the improved carrier delocalization, recombination resistance, and charge transfer properties in the composite system through Z-scheme formation. Parametric investigations by varying the concentration of catalyst, dye, and pH along with recycle studies, demonstrated the excellent stability of the developed composites for sustainable photocatalytic applications.

Water contamination from various sources, especially industrial waste containing hazardous dyes and heavy metals, has become a global environmental issue demanding urgent attention[1]. Conventional wastewater treatment methods like reverse osmosis, coagulation, and filtration have limitations such as byproduct formation and inadequate degradation or conversion efficiencies, making them unsuitable for long-term solutions[2]. Hence, there is a pressing need for alternative, cost-effective, and sustainable wastewater treatment approaches. Photocatalysis, a green technology that harnesses renewable solar energy, has gained significant momentum as an emerging solution[3]. The conventional photocatalysis process involves photoexcitation of the target photocatalyst under solar irradiation, leading to the generation and separation of charge carriers, which then migrate to the surface and participate in the desired redox reactions[4]. An ideal photocatalyst should possess a visible light-responsive bandgap, high photon harvesting efficiencies, efficient charge carrier mobility, low recombination rates, and abundant active surface sites for fast reaction and adsorption. Over the past four decades, various semiconductor photocatalytic materials have been explored and extensively studied[5,6]. While many of the materials have proven effective as photocatalysts, they face drawbacks such as poor chemical stability, high recombination rates, inefficient charge separation, and limited surface reactive sites, hindering their practical applications. Most

Centre for Nano and Material Sciences, Jain (Deemed-to-be University), Jain Global Campus, Kanakapura, Bangalore, Karnataka 562112, India. $^{\boxtimes}$email: m.sakar@jainuniversity.ac.in; br.geetha@jainuniversity.ac.in

importantly, the crucial requirement of a visible light-responsive bandgap is not met by many of these materials, prompting the ongoing search for an ideal photocatalyst[7–9]. In this direction, metal–organic frameworks (MOFs), a class of porous polymer-based materials composed of modifiable multidentate organic ligands connected to metal centers (metal-oxo clusters), have gained growing attention in the field of photocatalysis due to their inherent large specific surface area, desirable topology, and tunable pore structure[10]. However, MOF-based photocatalysts still face challenges such as low solar energy conversion efficiency, low conductivity, and rapid electron–hole pair recombination, impacting their performance. To overcome these limitations, compositing MOFs with other photocatalytic semiconductors is considered a promising alternative[11,12].

Among various photocatalytic materials, two-dimensional graphitic carbon nitride (g-C_3N_4), a metal-free visible light-active photocatalyst, is considered the most stable allotrope. A major advantage of g-C_3N_4 (GCN) is its straightforward synthesis method, where nitrogen-rich precursors undergo thermal condensation to form GCN[13]. It possesses unique electronic band structures, a non-toxic elemental composition, and high thermal and chemical stability across a wide range of pH conditions. Its notable visible light absorption property makes it highly suitable for visible light-driven photocatalytic applications. However, limitations such as fewer surface reactive sites, high charge recombination, and inferior charge separation hinder GCN's effectiveness as an individual photocatalyst[14]. The formation of composites between MOFs and GCN can help overcome these limitations through synergistic effects. For instance, Li et al. used g-C_3N_4 with NH_2-MIL-88B (Fe) as a heterojunction photocatalyst for MB degradation, and the degradation rate reached almost 100% after 120 min[15]. Huang et al. prepared g-C_3N_4/MIL-53 (Fe) heterojunction for improving the photocatalytic efficiency of Cr (VI) reduction, which displayed about 2.1 and 2.0 times than that of g-C_3N_4 and MIL-53 (Fe), respectively[16]. Du et al. fabricated MIL-100 (Fe)/g-C_3N_4 composites with heterostructures by ball-milling and annealing, which exhibited photocatalytic efficiency of Cr (VI) reduction reached up to 97% within 80 min, in addition, diclofenac sodium degradation reached ~ 100% within 50 min after adding H_2O_2[17]. NH_2-UiO-66 (Zr) is emerging as a hot-spot MOF, composed of Zr^{4+} as metal-oxo clusters and 2-aminoterephthalic acid (NH_2-BDC) as linkers, which exhibits excellent chemical stability and hydrothermal stability in a wider pH range, thus receiving extensive attention[18]. However, the insights into the synergetic properties of Ni-based MOFs, g-C_3N_4, and its composites are relatively less discussed in the literature. In this context, this study reports the synthesis of Ni-based MOFs with different organic ligands, namely terephthalic acid and 2-aminoterephthalic acid, and their integration with g-C_3N_4 using a facile single-step hydrothermal method. The bare MOFs, g-C_3N_4, and the composites with different ligands are investigated for their photocatalytic ability to degrade rhodamine B (cationic) and Congo red (anionic) dyes as model pollutants under natural sunlight irradiation. It can be seen that this work is particularly novel, as there are limited reports on the photocatalytic degradation using the specific combinations of Ni-MOFs with different ligands incorporated into g-C_3N_4 to construct Z-scheme-based composites for photocatalytic applications.

Experiment

Materials

All the chemicals used for synthesizing the Ni-MOF, GCN, and their composite systems were of analytical grade with a purity of ~ 99% and were used as purchased. These chemicals included nickel (II) nitrate hexahydrate ($Ni(NO_3)_2 \cdot 6H_2O$) (Avra Chemicals), benzene-1,4-dicarboxylic acid (H_2BDC) (Avra Chemicals), 2-amino terephthalic acid ($C_8H_7NO_4$) (Sigma Aldrich), N, N dimethylformamide (DMF, C_3H_7NO) (Avra Chemicals), melamine ($C_3H_6N_6$) (Sigma Aldrich), rhodamine B (RhB) (Sisco Research Laboratories Chemicals), and congo red (CR) (Sisco Research Laboratories Chemicals).

Synthesis of Ni-MOFs with different ligands

In a typical synthesis process of Ni-MOFs, 0.12 mmol of nickel nitrate hexahydrate ($Ni(NO_3)_2 \cdot 6H_2O$) was dissolved in 40 mL of dimethylformamide (DMF), resulting in solution A. Concurrently, an equivalent quantity (0.12 mmol) of either terephthalic acid or 2-amino terephthalic acid ligand was dissolved in another 40 mL of DMF, forming solution B. Each solution was stirred separately for 30 min. Following this, solution B was added drop-wise to solution A and stirred for an additional 20 min. This solution mixture was then moved into a Teflon-lined stainless-steel autoclave and heated in a hot air oven at 180 °C for 24 h. After the hydrothermal process, the solution was centrifuged, and the solid product was washed repeatedly with DMF and methanol to eliminate any remaining reagents and residues. The cleaned product was dried in a vacuum oven at 80 °C for ~ 12 h. The Ni-MOFs synthesized using terephthalic acid and 2-aminoterephthalic acid were named NTP and NATP, respectively[19].

Synthesis of g-C_3N_4 (GCN)

The synthesis of g-C_3N_4 (GCN) was carried out using a thermal condensation technique with melamine serving as a precursor material. In this process, 5 g of melamine was loaded in an alumina crucible with a lid and subjected to calcination at a temperature of 550 °C for a span of 4 h. The rate of heating was kept constant at 5 °C per min in a programmable muffle furnace. After the furnace cooled down to room temperature, the resulting pale-yellow solid was ground into a fine powder and preserved for subsequent use and analysis[20].

Synthesis of Ni-MOF/GCN composites

The Ni-MOF/GCN composites were synthesized using the solvothermal method. In a typical synthesis procedure, an equal quantity of (0.12 mmol) nickel nitrate hexahydrate ($Ni(NO_3)_2 \cdot 6H_2O$) and either terephthalic acid or 2-amino terephthalic acid ligand was mixed in 40 mL of DMF and stirred for 20 min. Following this, 0.5 g of the previously synthesized GCN was dispersed into the solution, followed by 30 min of sonication. The solution was then transferred into a Teflon-lined stainless-steel autoclave and heated in a hot air oven at 180 °C for 24 h. The

resulting solution was centrifuged and dried at 80 °C for 12 h. The composites synthesized using terephthalic acid and 2-amino terephthalic acid-liganded Ni-MOFs were named NTP/GCN and NATP/GCN, respectively[21,22].

Characterizations

X-ray diffraction patterns were obtained using Rigaku's Ultima-IV X-ray diffraction instrument equipped with CuK radiation (λ = 1.5406 Å). The XRD pattern was recorded in the 2θ range 5–80° at a scan rate of 5°/min. Diffuse reflectance spectra (DRS) were recorded using a UV–Vis absorption spectrophotometer (PerkinElmer, Lambda 365, UV–Vis-DRS) in the range of 190–900 nm with an integrating sphere attachment and BaSO$_4$ as a reflectance standard. The structural morphology and element distribution of the synthesized samples were studied by using field emission scanning electron microscopy (JEOL model JSM7100F), and HRTEM (Thermofisher, model Talos F200 S) combined with energy dispersive spectroscopy (EDS). Brunauer–Emmett–Teller (BET) analysis and the Barrett-Joyner-Halenda (BJH) method were used to analyze the N$_2$ adsorption and desorption behavior, pore distribution, and surface area using BET BELSORP Max, Japan. A Shimadzu RF-5301PC spectrofluorophotometer was used to carry out the PL analysis with a 150 W xenon lamp at an excitation of 460 nm. X-ray photoelectron spectroscopy (XPS) analysis was conducted with an ESCA + photoelectron spectrometer from Omicron Nanotechnology, Oxford Instruments, and using mono-chromated aluminum (Al-Kα) as the radiation source. All electrochemical measurements were performed using a CHI660D potentiostat (CH Instruments, Austin, USA) in a standard three-electrode system (CHI) with modified 3 mm diameter glassy carbon as working electrode, platinum wire as a counter electrode, and Ag/AgCl (1 M KCl) as a reference electrode.

Photocatalytic experiments

In the standard dye degradation procedure, a stock solution was prepared by dissolving 10 mg of RhB and CR dye in 1 L of double-distilled water to prepare 10 ppm concentrated dye solutions. From this stock, 100 mL of dye solution was transferred to a 250 mL glass beaker. Then, an optimized concentration of 20 mg of photocatalyst was added and stirred for around 30 min in darkness to achieve a uniform dye-photocatalyst dispersion before exposure to sunlight. Then this reaction mixture was exposed under sunlight and gently stirred during the photocatalytic reaction to maintain the dispersion of the catalyst. At 30 min intervals, a 3 mL sample was pipetted out, and suspended particles were separated. The supernatant containing the degraded dye was collected, and its optical density was measured using an UV–vis spectrophotometer to determine dye degradation[23,24]. The photocatalytic properties of the best-performing NATP/GCN photocatalyst were investigated through parametric studies involving varying concentrations of catalyst (10, 20, and 30 mg), dyes (5, 10, and 20 ppm), and different pH conditions (5, 7, and 10).

Result and discussion

Structural analysis

The X-ray diffraction (XRD) patterns of the synthesized Ni-MOFs with different ligands such as terephthalic acid (NTP) and 2-amino terephthalic acid (NATP), g-C$_3$N$_4$ (GCN), and their composites (NTP/GCN and NATA/GCN) with 2θ ranges of 5–55° and 24–31°, respectively are provided in Fig. 1a, b.

The XRD patterns corresponding to NTP and NATP samples confirm the formation of Ni-MOF with the corresponding terephthalic acid and 2-amino terephthalic acid ligands in the frameworks. In both cases, prominent diffraction peaks appeared at 2θ values of ~ 7.3, 8.4, 17.54, 25.3, 28.04, and 31.3° can be assigned to the planes (100), (110), (220), (210), (220), and (300), respectively[25,26]. The other minor diffraction peaks can be assigned to the short-range crystalline or disorder nature of the frameworks. Similarly, the diffraction peaks for GCN
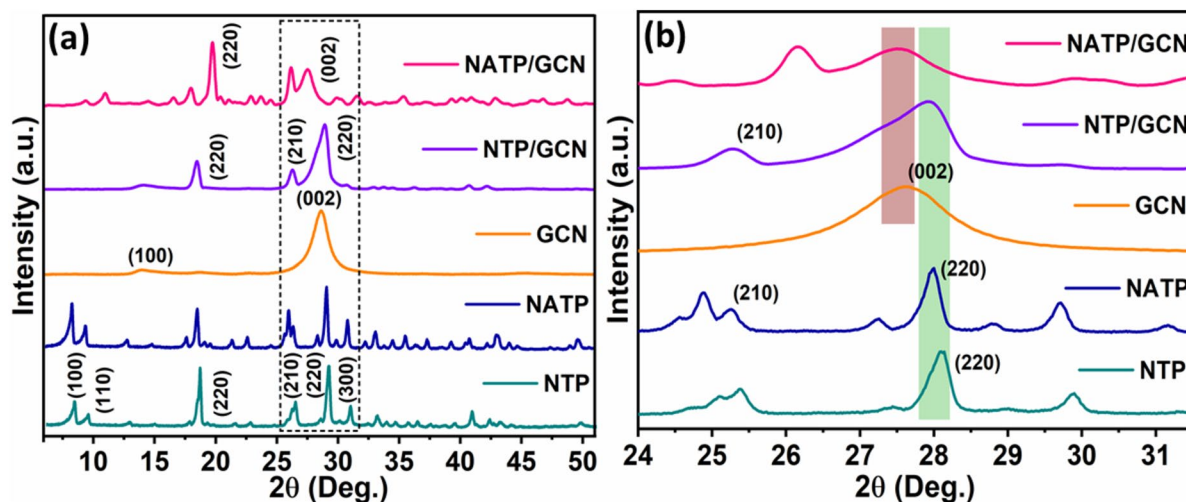
Fig. 1. (**a**) Full range and (**b**) zoom-in XRD patterns of the synthesized Ni-MOFs with different ligands, GCN, and their composites.

appeared at 2θ values of ~ 12.8 and 27.6°, corresponding to the (100) and (002) planes. This confirms the formation of the g-C$_3$N$_4$ phase of the carbon nitride system, which matches well with the JCPDS card #87-1526[27].

In the XRD pattern of NTP/GCN composite, the appearance of peaks corresponding to both NTP and GCN confirms the formation of the composite. Observations such as the merging of the major peaks of NTP (220) and GCN (002), along with changes in the peak positions and broadening relative to the corresponding bare systems (Fig. 1b), suggest active chemical interactions between the Ni-MOF and GCN through their functional groups. Similarly, all peaks corresponding to NATP and GCN are significantly deformed and shifted in the XRD pattern of the NATP/GCN composite. This indicates that interactions between the NATP-MOFs and GCN are stronger than those between NTP-MOFs with GCN, leading to robust coordination or hydrogen bonding and alterations in the packing arrangement of atoms in the crystal lattice of MOFs[28]. These structural features suggest that the NTP/GCN composite may exhibit collaborative properties, while the NATP/GCN composite exhibits synergistic properties due to robust chemical interactions between the NATP-MOFs and GCN systems.

Further, the crystallite size of the synthesized materials was estimated using Scherrer's formula (D = 0.9λ/βcosθ, where D is crystallite size (nm), 0.9 is crystallite shape constant, λ is the wavelength of X-rays used (Å), β is the full width at half maximum, and θ is the Bragg's diffraction angle (°)). The calculated crystallite sizes were around 19.2, 15.9, 6.5, 29.4, and 30.5 nm for NTP, NATP, GCN, NTP/GCN, and NATP/GCN, respectively. The observed increase in crystallite sizes of the composites compared to the bare materials indicates the presence of lattice-level interference between MOFs and GCN in the composites, facilitating overall crystallite growth in the system. These findings further confirm that both the MOFs and GCN are chemically connected and interacting within the composite systems[29].

Functional group analysis

The ATR-IR spectra of the synthesized NTP-MOFs, NATP-MOFs, bare-GCN, and their composites are shown in Fig. 2. Both NTP and NATP MOFs exhibit a strong peak around 1550 cm^{-1} corresponding to the carboxylic acid groups in the system. The bands around 2800 and 1400 cm^{-1} can be assigned to the C-H stretching and bending vibrations of the ligands[30]. Peaks in the 750–800 cm^{-1} region may be attributed to C–C stretching in aromatic rings. Low-frequency peaks indicate Ni–O-carboxylate interactions in these systems. A broad hump-like band around 3300 cm^{-1} is related to the O–H stretching vibrations of adsorbed water molecules in NTP MOFs, but it appears deformed in NATP MOFs due to the presence of amnio-groups in the system[31].

In the spectrum of g-C$_3$N$_4$, peaks in the 500–700 cm^{-1} range are assigned to C–N–C bending vibrations. Peaks in the 1500–1700 cm^{-1} range correspond to C–N and C=N stretching vibrations, while peaks in the 1440–1500 cm^{-1} region indicate C=C stretching vibrations. Further, a hump-like peak in the 3000–3300 cm^{-1} region suggests the presence of adsorbed water molecules, with C–H and N–H groups observed in the 700–1000 cm^{-1} region. The spectra of the composites (NTP/GCN and NATP/GCN) are found to be similar to the spectra of GCN, reflecting the vibration-structure dominance of GCN over the MOFs. Notably, the strong peaks corresponding to the carboxylic acid groups in MOF are also not present in the composite. This suggests that the carboxylic groups of MOFs are strongly influenced by the C–N network of GCN, leading to a stronger bonding between the two systems and stabilizing them into a composite. This could facilitate functional interactions within the composites. Particularly, since the MOF has metal centers capable of electron transfer, their interactions with GCN could lead to the formation of charge transfer complexes, thereby making the composite more physiochemically active systems for dynamic reaction environments[32,33].
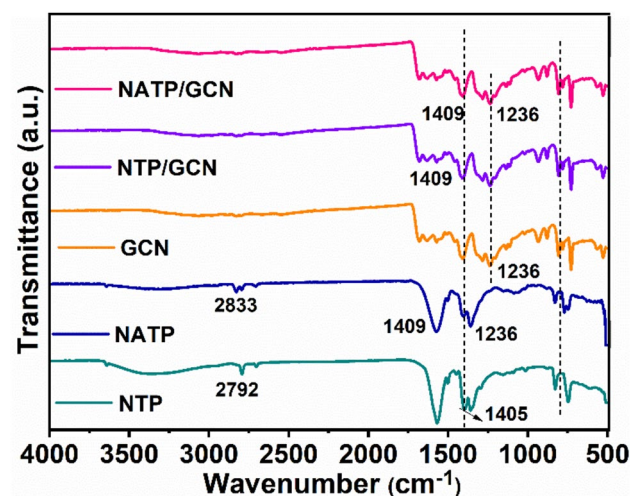

Fig. 2. ATR-IR spectra of the synthesized Ni-MOFs with different ligands, GCN, and their composites.

Morphology analysis

Morphological analysis by field emission scanning electron microscopy (FESEM) exhibited 2D-flakes like structure assembled into a flower-like structure for both NTP, and NATP-MOFs as shown in Fig. 3a, b. Similarly, an agglomerated particle-like structure was observed for GCN system, as shown in Fig. 3c. In the case of composite systems, the integral structures, reflecting the morphology of the respective individual system is observed[34]. Accordingly, a mixed particulate morphology of NTP and GCN is observed for the NTP/GCN composite (Fig. 3d), whereas the particles-decorated on a flower-like structure is observed for the NATP/GCN composite as shown in Fig. 3e. The EDS elemental mapping of NATP/GCN composite (Fig. 3f–i) confirmed the presence of the respective elements in the system[35]. The observed irregular particle and flower-like morphology of NTP and NATP MOFs, respectively, can be attributed to the binding habit of the respective ligands on the growing Ni particles, forming the frameworks and the materials' morphology. The terephthalic acid (TP) has a symmetric, planar structure with two carboxylic acid groups (–COOH) at opposite ends of the molecule. Therefore, their coordination with Ni ions may not favor a specific crystallographic direction for growth and binding, leading to the formation of irregular-particles.

On the other hand, 2-aminoterephthalic acid (ATP) contains an amino group (–NH$_2$) in addition to carboxylic acid groups[36]. This additional functional group introduces asymmetry and additional binding sites for coordination with metal ions, allowing for more diverse interactions and control over crystal growth. As a result, this can alter the coordination environment around metal ions and influence direction growth of the crystals. This can lead to the formation of well-defined facets or specific crystallographic orientations, which are conducive to the development of flower-like morphologies. Moreover, the amino group in ATP can also participate in hydrogen bonding or other supramolecular interactions that promote the self-assembly of MOF units into hierarchical structures, such as the petals of a flower, during crystal growth[37].
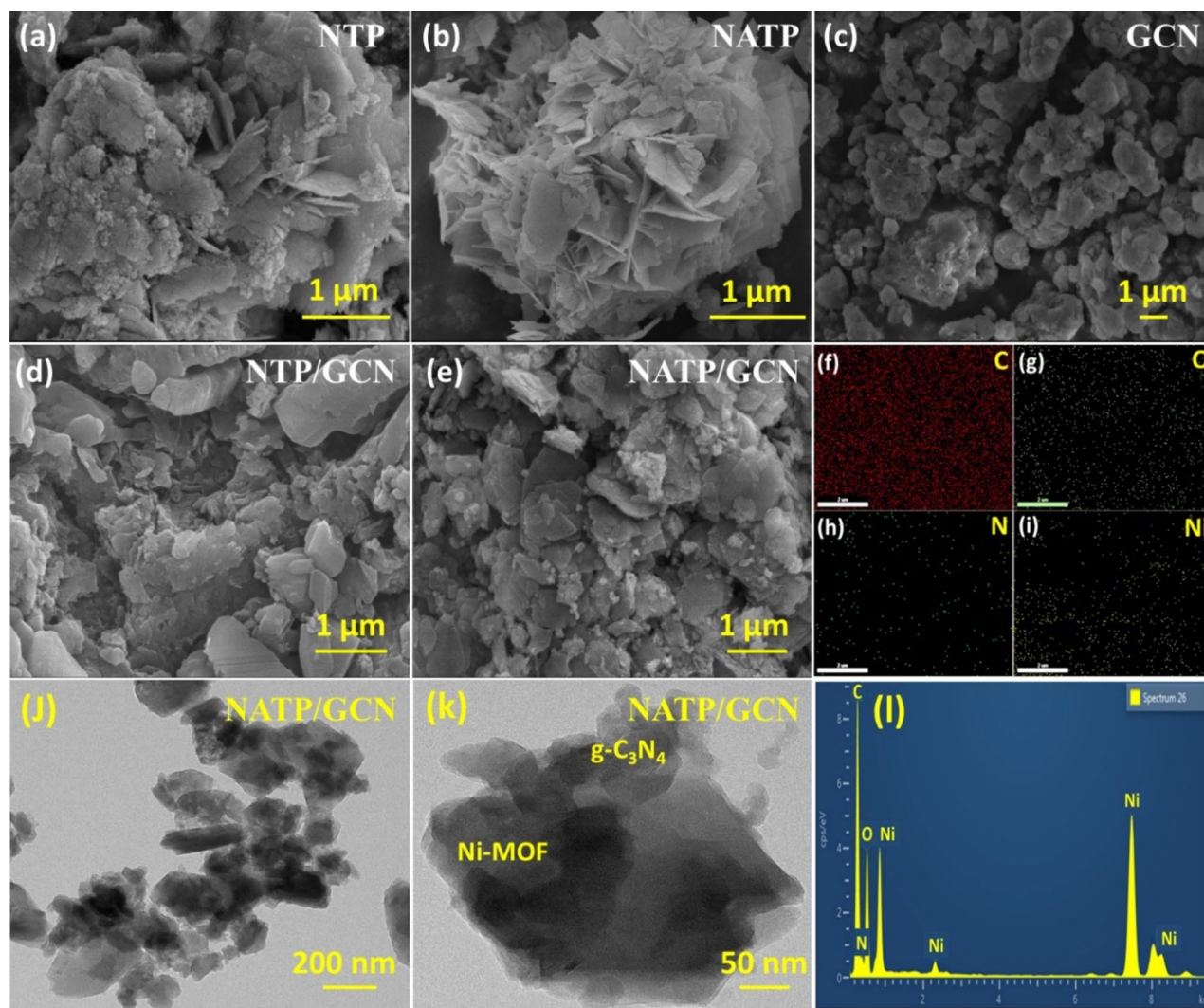
Fig. 3. FESEM image of the synthesized (**a**) NTP-MOF, (**b**) NATP-MOF, (**c**) GCN, (**d**) NTP/GCN, (**e**) NATP/GCN composites, (**f**)–(**i**) EDS elemental mapping images of NATP/GCN composite, (**j**), (**k**) TEM image of NATP/GCN composites, and (**l**) EDS elemental spectrum of NATP/GCN composite.

These features of the resulting NTP and NATP MOFs are found to be inherited during the composite formation with GCN. Accordingly, an integrated particulate-like morphology with non-uniform shape is observed for NTP/GCN composite[38]. In contrast, the GCN particles are found to be well intercalated in between the flakes of NATP MOF flowers, leading to the formation of particles-decorated flower-like morphology for NATP/GCN composite. These observations suggest that the active sites of NATP facilitate the deposition of GCN particles onto their surface, which keeps the composite more functional compared to the NTP/GCN composite. This hierarchal anisotropic structure of NTP/GCN composite inherits and improves the properties of MOFs via interacting with the GCN and vice versa, thereby manifesting synergistic properties in the system[39].

The morphology and the EDS spectrum of the NATP/GCN composite were further examined using high-resolution transmission electron microscopy (HRTEM), with the resulting images shown in Fig. 3j–l. The TEM images clearly illustrate that the GCN are not merely attached to the surface but are embedded within the NATP matrix with average size of 100 nm as shown in Fig. 3j, k. Further, it confirms the co-existence of both NATP MOF and GCN, which can be distinctly identified by their characteristic morphological features, as illustrated in Fig. 3k. The intercalation of GCN on the flakes of the Ni-MOF is also observed, indicating a strong interaction between the two components, promoting a uniform and stable composite. This suggests that the NATP MOF offers a favorable environment for the deposition and stabilization of GCN, likely due to its abundant active sites. These active sites are crucial as they facilitate the anchoring of GCN onto the NATP surface, ensuring that the composite maintains its functional integrity which leads to a synergistic effect[40]. Further, the characteristic presence of elements such as C, O, N, and Ni in the formed NATP/GCN composite is evidenced in the EDAX spectrum as shown in Fig. 3l.

Optical properties

The UV–visible absorption spectra of NTP and NATP MOFs exhibit a couple of absorption peaks in the UV region around 320 and 375 nm with absorption edge in the range of 430–450 nm as shown in Fig. 4a. The observed optical absorption in the UV and visible light region can be typically attributed to the electronic transitions such as ligand-to-ligand and ligand–metal charge transfer, respectively in the systems. Similarly, the absorption peak at ~388 nm with an absorption edge around 475 nm is observed for GCN, attributed to the electronic transitions between the HOMO–LUMO energy levels. In the case of NTP/GCN composite, the absorption peaks at 327 and 374 nm are observed, where the intensity of the latter peak is improved. This can be attributed to the effective optical interaction of NTP MOFs with GCN in the composite. On the other hand, the spectrum of NATP/GCN composite is found to exhibit an improved absorption peak at 376 nm, reflecting the dominant properties of GCN in the composite, which is crucial for the improved light harvesting for photocatalytic reactions.

The bandgap energy of NTP, NATP, GCN, NTP/GCN, and NATP/GCN was estimated from the Tauc's plots as shown in Fig. 4b and a corresponding value of 2.93, 2.74, 2.77, 2.76, and 2.70 eV was obtained. The estimated band gap energy values are in accordance with their absorption spectra, indicating the UV–visible light driven band gap energy of the materials. Upon integrating the NTP and NATP MOFs with GCN, the band gap energy of both the composites is decreased to around 2.76 and 2.70 eV, respectively, indicating that the energy levels of both the systems are involved in the making of HOMO–LUMO energy levels of the composites. This clearly indicates that the electronic transitions and the subsequent improved optical features are facilitated in the composites since both MOFs and GCN are integrated through chemical interactions, leading to the synergistic properties in the systems[41].

The photoluminescence (PL) spectra obtained under an excitation wavelength of 320 nm exhibited a peak around 430 nm for both NTP and NATP MOFs as shown in Fig. 5. The observed enhanced PL intensity for NTP MOFs indicates that this system has an effective excitation and carrier recombination pathways during
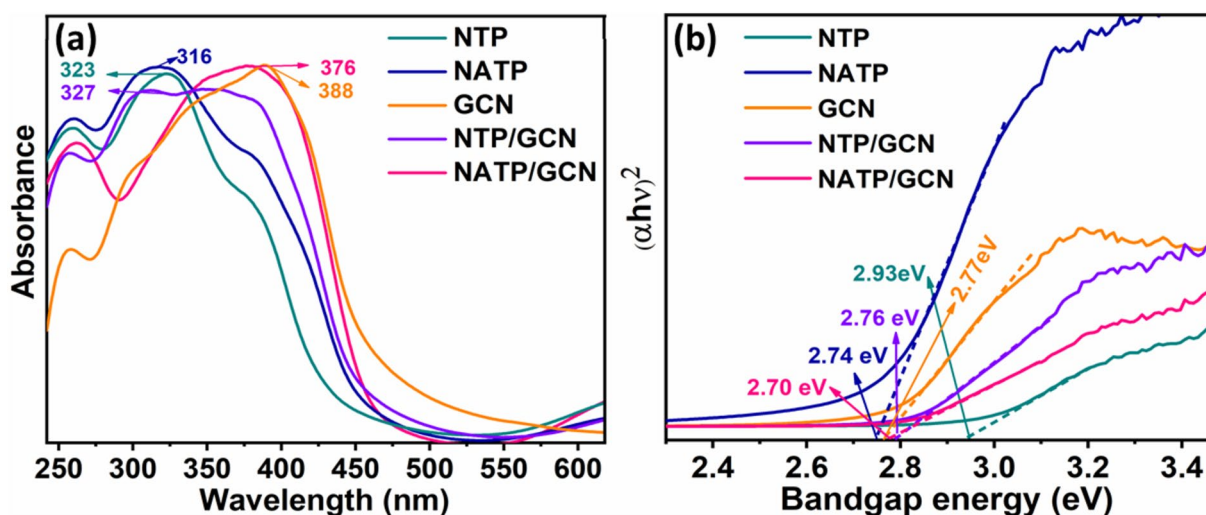
Fig. 4. (a) UV–Visible absorption spectra, and (b) Tauc's plot for bandgap estimation of Ni-MOF with different ligands, GCN, and their composites.
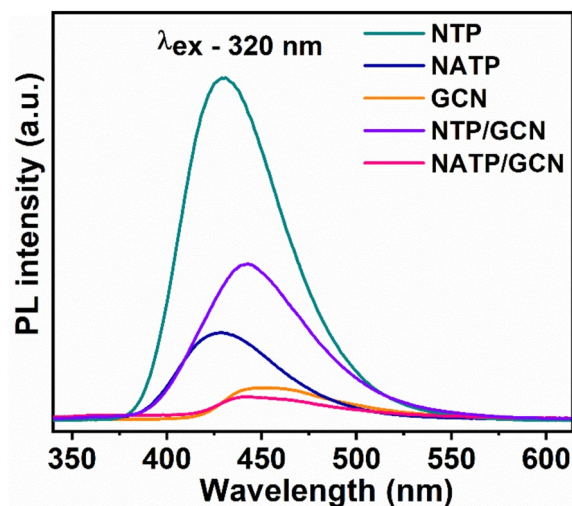
Fig. 5. Photoluminescence spectra of the synthesized Ni-MOFs with different ligands, GCN, and their composites.

photoexcitation process. Conversely, the PL intensity is found to be decreased for NATP MOFs, attributed to the presence of amino groups interacting in the bandgap structure and leading to increase the recombination resistance in the system.

A significant decrement in the PL intensity is observed for GCN, which suggests that this system intrinsically possesses a band gap structure conducive for the carrier excitation and resistive towards charge recombination[42]. Accordingly, upon integration of GCN, the PL intensity of NTP/GCN composite is further decreased considerably compared to bare NTP, whereas, it is drastically decreased for NATP/GCN composite. Also, the peak positions are found to be red-shifted, indicating their short carrier pathways. These observations suggest that the charge recombination process in these composites is greatly decreased, which can in turn make the charge carriers available more on the surface for the effective chemical reactions[43]

Surface properties

The surface sorption characteristics of the NTP/GCN and NATP/GCN composite were investigated by recording the BET-N_2 gas adsorption–desorption hysteresis curves as shown in Fig. 6a. Both the systems exhibit the typical type III isotherms, which indicates the microporous or mesoporous properties of the materials. According to this type, both adsorption and desorption is gradual in the material, while a steep-increase is observed at higher pressures. This indicates that the adsorbates stay in the material surface upon high pressures or such similar environments. These characteristics are highly important for a photocatalyst to facilitate the pollutant removal through degradation rather than merely adsorbing them. This eventually improves the reusability and regeneration of the photocatalysts for sustainable process[44].
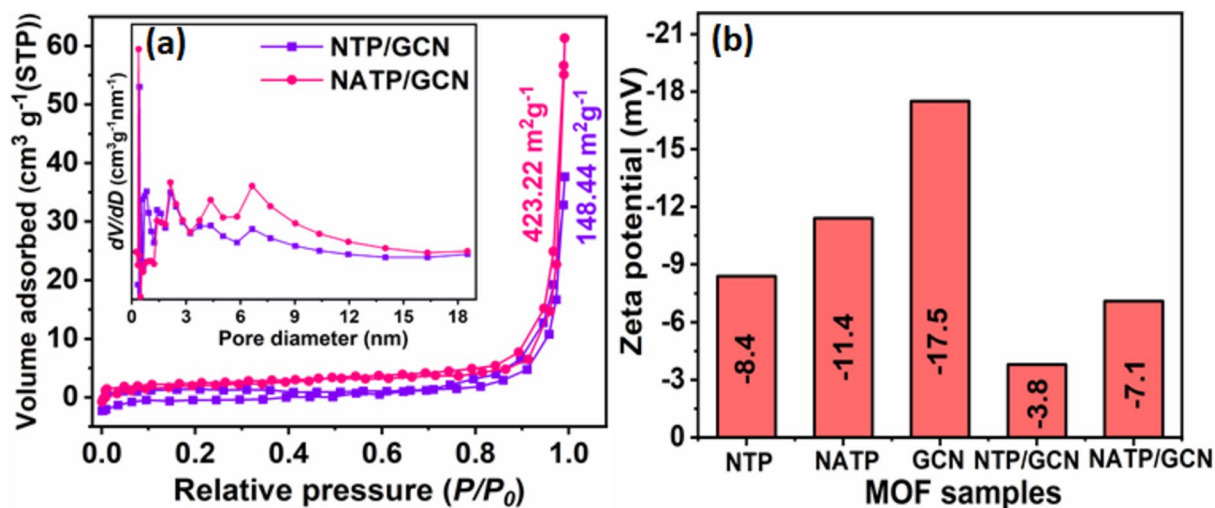

Fig. 6. (**a**) Nitrogen adsorption–desorption isotherms and (**b**) Zeta potential graphs of the synthesized Ni-MOFs with different ligands and their composite with GCN.

From the BET curves, a surface area of ~ 148.4 and 423.2 m² g⁻¹ was estimated for NTP/GCN and NATP/GCN composite, respectively. The observed higher surface area of NATP/GCN composite can be attributed to the amino groups in the MOFs, which can facilitate the creation of more binding sites and increase the overall porosity of the composite material. This can be validated from the observed increased pore size of (~ 2.7 nm) compared to NTP/GCN composite (~ 1.8 nm). Also, the ATP ligands in the composite can lead to stronger interactions with GCN leading to have more open accessible porous structure in the composites and contributing to the enhanced surface area[45].

The surface zeta potential all the systems is found to be negative, originated due to the carboxylate groups (–COO⁻) of both NTP and NATP MOF, thereby in the composites as shown in Fig. 6b. The obtained higher negative zeta potential of NATP MOF (− 11.4 mV) compare to NTP MOF (− 8.4 mV) can be attributed to its amino (– NH₂) groups, which contributes to a greater overall negative charge on the surface of the NATP MOF, leading to a more negative zeta potential. Similarly, the GCN contains functional groups such as amine (–NH₂) and amide (–CONH⁻) groups on its surface leading to the negative zeta potential of the material. On the other hand, upon the composite formation, the negative charge of the composites is considerably decreased to around − 3.8 and − 7.1 mV for NTP/GCN and NATP/GCN composite, respectively. This can be attributed to the electrostatic interaction between the materials, leading to shielding effect where the repulsion between the negatively charged surfaces can be partially neutralized by the attractive forces between them, resulting in a decrease in the overall repulsive forces and thus a decrease in the zeta potential. It may also be possible that the negatively charged g-C₃N₄ particles interacting with some of the positively charged species in the Ni-MOFs, leading to decrease in the overall zeta potential of the composites. Moreover, the strong bonds or complex formation between the materials can also alter the distribution of charges or reduce the availability of charged sites, it can lead to a decrease in the overall negative charge of the composite[46].

XPS analysis

The presence and oxidation states of elements in the NATP/GCN composite were analyzed using X-ray photoelectron spectroscopy (XPS). The narrow scan spectra for Ni, O, C, and N are displayed in Fig. 7a–d. The Ni 2p spectrum (Fig. 7a) shows peaks at 856.8 eV and 873.2 eV, corresponding to the Ni 2p$_{3/2}$ and Ni 2p$_{1/2}$ orbital
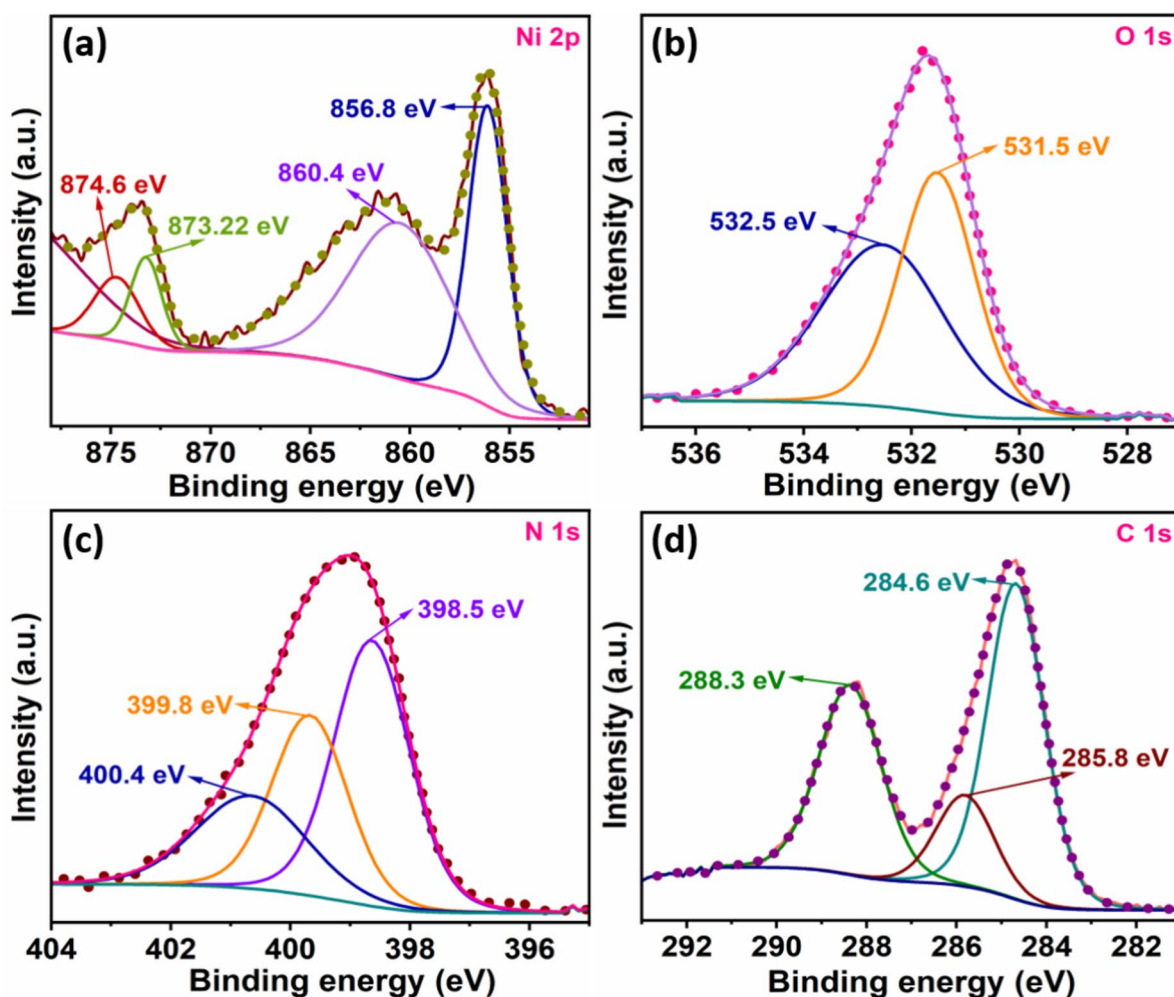

Fig. 7. High-resolution XPS spectra of (**a**) Ni 2p, (**b**) O 1 s, (**c**) N 1 s and (**d**) C 1 s in NATP/GCN composite.

binding energies, which represents the + 2 oxidation state of Ni ions in the composite system[47]. The deconvoluted peaks around 860.4 eV and 874.6 eV associated with broad satellite peaks of Ni $2p_{3/2}$ and Ni $2p_{1/2}$, respectively. The O 1 s spectrum is found to be asymmetric (Fig. 7b), with a major peak at 531.7 eV corresponding to the lattice oxygen (O_L) in the system, indicated its O^{2-} oxidation state[19], while the deconvoluted peaks at 531.5 and 532.5 eV could be assigned to the existence of non-lattice oxygens such as oxygen vacancy (O_V) and adsorbed oxygen (O_{ads}), respectively, in the composite system[57]. The N 1 s spectrum (Fig. 7d) is also asymmetric, with a major peak at 398.9 eV attributed to the triazine cyclic unit (C=N–C) in the g-C_3N_4 system. A secondary deconvoluted peak at 400.4 and 399.8 eV corresponds to tertiary nitrogen atoms in the C–N–C–C network of the polymeric g-C_3N_4[48]. The C 1 s spectrum (Fig. 7c) shows peaks at 284.7 eV and 288.3 eV, indicating sp^2 C–C bonds and sp-carbon bonds in nitrogen-containing aromatic networks (N=C–N) within the g-C_3N_4 system[49]. These results confirm that the elements in the synthesized NATP/GCN composite exist in their stable oxidation states, ensuring the formation of an active metal–organic framework/g-C_3N_4 composite.

Photocatalytic studies

The photocatalytic efficiencies of the developed bare and composite materials towards degradation of rhodamine B (RhB) and Congo red (CR) dyes are investigated under sunlight irradiation and the obtained C/C_0 plots are provided in Fig. 8a, b. At the end of 120 min, the NTP, NATP, GCN, NTP/GCN, and NATP/GCN degraded the around 43/48, 79/60, 60/43, 67/57, and 93/64% of RhB/CR dyes, respectively. No degradation of dyes was observed in the absence photocatalysts, indicating that the degradation via photolysis of dyes is hardly possible. On the other hand, under dark condition, all the bare and composites generally show a minimal adsorption towards RhB and CR dye. However, the NTP/GCN and NATP/GCN composites show some considerable adsorption up to 20–35% towards CR dye.

As known, the Congo red is an anionic dye with sulfonate groups that carry negative charges in aqueous solutions[50]. Similarly, the composites carry a negative surface due to their functional groups. Upon contact, the negative charges of both the systems get homogenized, thereby the composites adsorb the dye molecules.
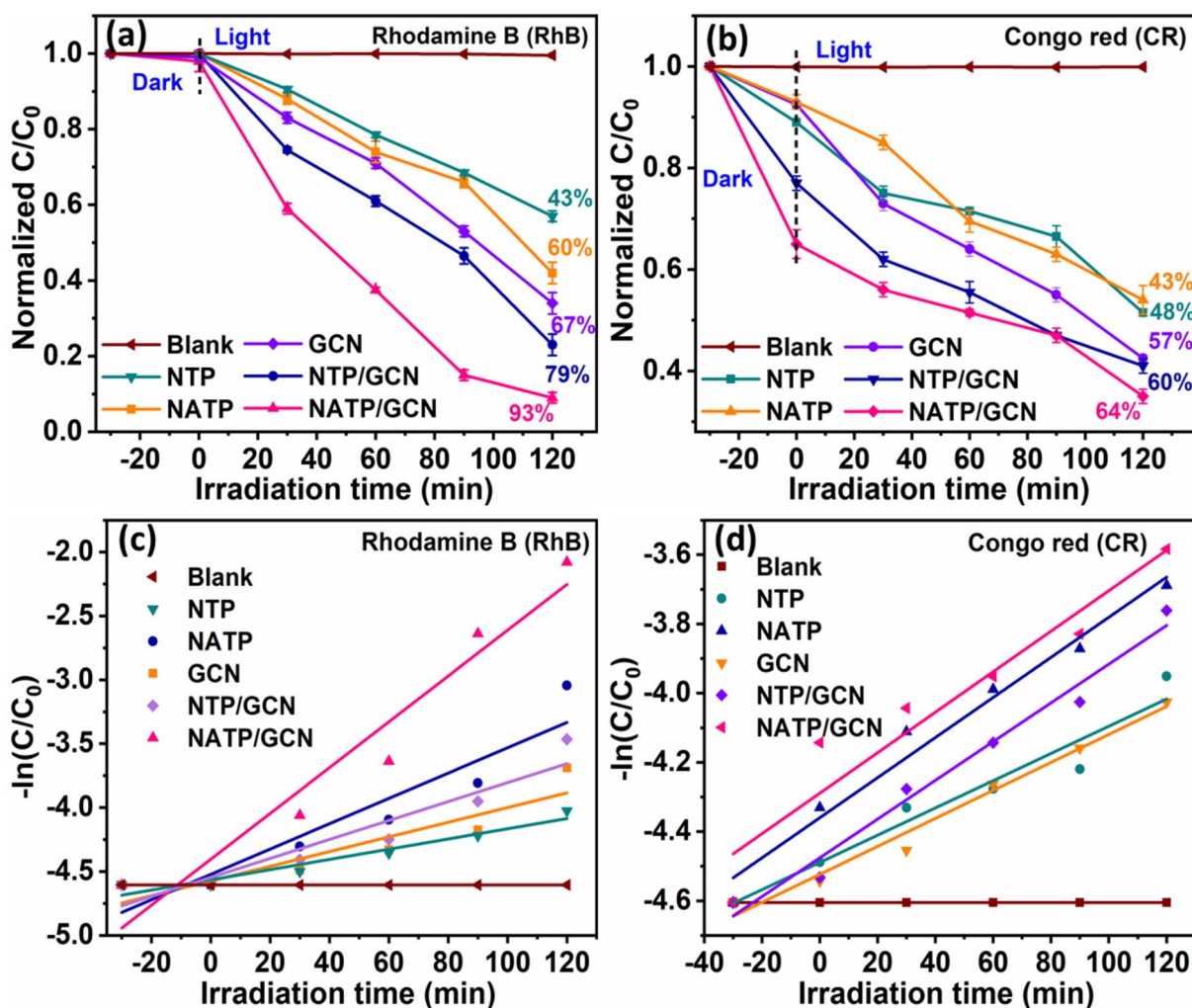
Fig. 8. C/C_0 plots of (**a**) RhB, (**b**) CR dye degradation, in the presence of Ni-MOFs with different ligands and their composite with GCN, (**c**), (**d**) Plots of $-\ln(C/C_o)$ versus irradiation time of the various synthesized materials in the degradation of RhB and CR dyes.

However, this observation also suggests that apart from the typical electrostatic interaction, the functional groups in the systems (especially in the composites) capable of forming hydrogen bonds or π-π interactions with the dye molecules, which can contribute to the adsorption of dye molecules irrespective of their positive or negative charges[51]. These observed enhanced photocatalytic efficiencies of the composites can be attributed to their greater abilities to produce photogenerated charge carriers and inter-transfers leading to their migration to the surface to produce active radicals and degrade the dyes.

The kinetics of the reaction during the degradation of RhB and CR dyes by various developed photocatalyst were evaluated by plotting $-\ln(C/C_0)$ as a function of time, as shown in Fig. 8c, d. The observed linear plots indicated that all systems follow first-order reaction kinetics. Accordingly, the rate constants (k) for the photocatalytic reactions over MOFs, and its composite were calculated. For RhB dye, the rate constants were determined to be around 0.24, 0.59, 0.34, 0.44, and 1.07 h^{-1} for NTP, NATP, GCN, NTP/GCN, and NATP/GCN composites, respectively (Fig. 8c). The enhanced efficiency of the NATP/GCN composite is reflected in its higher rate constant. For the CR dye, the rate constants were found to be around 0.23, 0.34, 0.24, 0.33, and 0.374 h^{-1} for NTP, NATP, GCN, NTP/GCN, and NATP/GCN composites, respectively (Fig. 8d). The NATP/GCN composite exhibits the highest rate constants for both RhB (1.07 h^{-1}) and CR (0.374 h^{-1}) dyes. In contrast, bare NTP and GCN show relatively lower rate constants for both dyes, which can be attributed to their limited light absorption and less effective charge separation compared to the composite materials. The NTP/GCN composite shows an improvement over the individual components, with rate constants of 0.44 h^{-1} for RhB and 0.33 h^{-1} for CR degradation. This improvement indicates a synergistic interaction between NTP and GCN, although it is less pronounced compared to the NATP/GCN composite. In order to gain further insights into the underlying mechanism of the observed photocatalytic properties of the systems, the Mott–Schottky and scavenger analyses were performed as discussed in the section "Mott–Schottky and electrochemical impedance analysis". Also, a table comparing the photocatalytic efficiency of the present material with other MOF/GCN-based composite photocatalysts reported in the literature is provided in Table 1 [16,52–60].
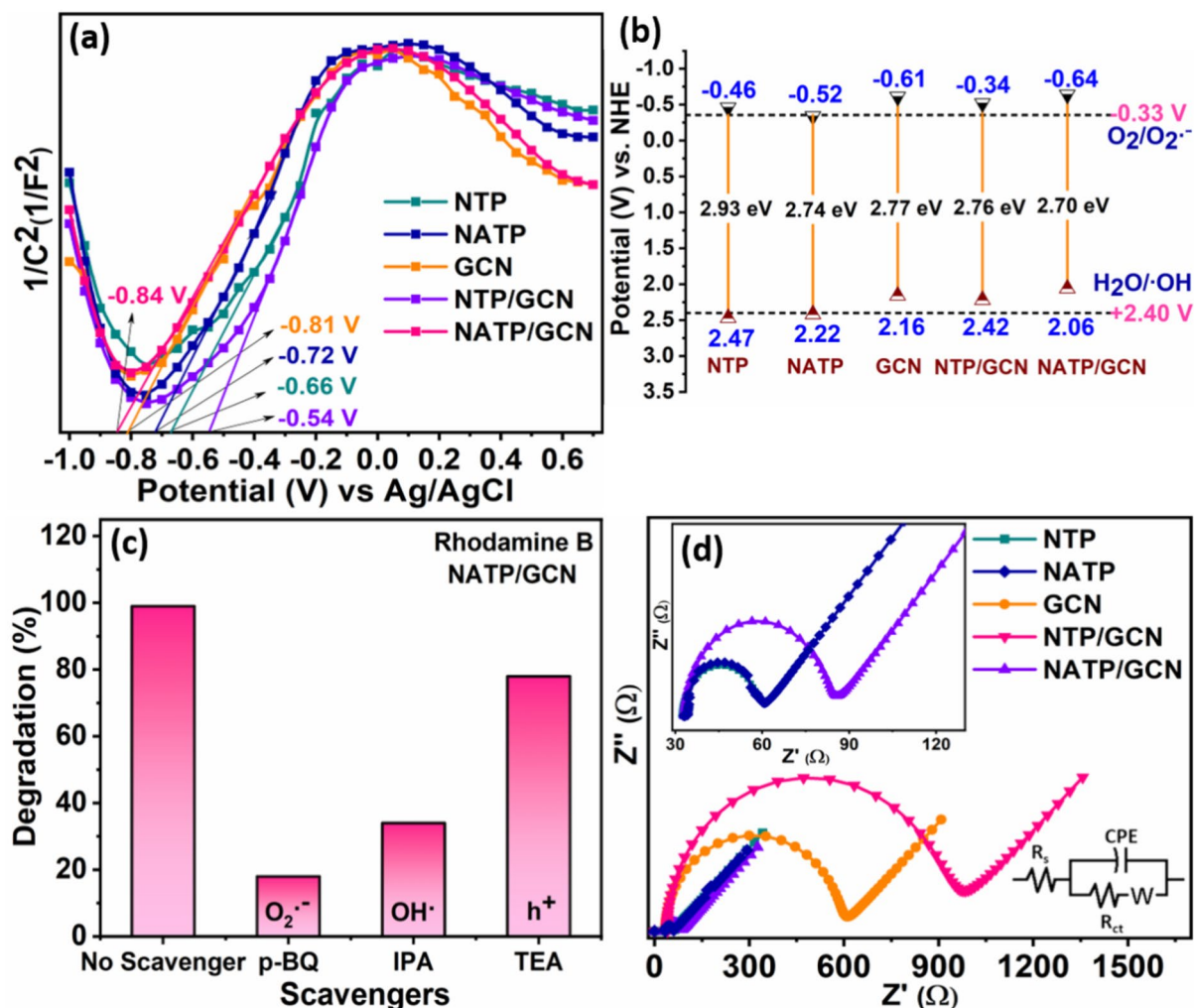
Mott–Schottky and electrochemical impedance analysis

The valence band (VB) and conduction band (CB) potentials of the developed photocatalysts were estimated with the help of Mott–Schottky (MS) analysis. From the obtained MS plots as shown in Fig. 9a, a flat-band potential values of -0.66, -0.72, -0.81, -0.54, and -0.84 V were estimated for NTP, NATP, GCN, NTP/GCN, and NATP/GCN, respectively. These negative values indicate the n-type conductivity of these systems, and thereby, their CB potential positions 0.2 V lower the flat-band potential. Accordingly, a CB value of -0.46, -0.52, -0.61, -0.34, and -0.64 V was calculated for the respective system. From the calculated band gap energy and CB values, a corresponding VB potential value of 2.47, 2.22, 2.16, 2.42, and 2.06 V was calculated using the formula $E_{VB} = E_g + E_{CB}$. Based on these values, the band structure of the synthesized materials is depicted in Fig. 9b. From the results, in general, the band structure of NTP and NTP/GCN composite is found to be more suitable for dye degradation with respect to the redox potential for the production of superoxide and hydroxyl radicals. In contrast, the other systems show enhanced reduction potentials suitable for the production of superoxide radicals, but unsuitable for the production of hydroxyl radicals. However, the photocatalytic efficiency depends on several parameters including having a suitable band gap energy, improved charge carrier separation, and rapid carrier transfer to the surface to involve in the redox reactions[61].

To further probe into the generation of radical species, the scavenger experiments, by employing TEA, IPA, and p-BQ as a scavenger for h$^+$, OH· and O$_2$·$^-$ radicals respectively, were performed during the photocatalytic degradation of RhB dye by NATP/GCN composite. From the results obtained (Fig. 9c), the photocatalyst showed a maximum degradation of dye when no scavenger was present and it was slightly decreased when TEA was added, indicated the degradation of dye via direct hole-oxidation reaction. Upon introducing p-BQ and IPA, the

Photocatalyst	Organic dye	Light source	Conc. of photocatalyst (mg/mL)	Dye Conc. (ppm)	Degradation (%)/Time (min)	References
Ce-MOF/g-C$_3$N$_4$	MB	Visible light (Xe)	10/100	10	96.5/120	52
α-Fe$_2$O$_3$/g-C$_3$N$_4$	RhB/CV	Sunlight	10/50	10	93/95/150	53
Fe-MOF/g-C$_3$N$_4$	MB	UV–Visible light	20/100	20	71.2/120	54
Ni-MOF@ BiOBr composite	MB	Visible light	10/100	20	92.8/120	55
Ni-MOF	CV	Sunlight	20/100	20	93/30	56
Ni-MOF/g-C$_3$N$_4$	CV	Visible light (Xe)	20/100	20	90/120	57
NH$_2$/MIL-88B(Fe)	CR	Visible light (Xe)	10/50	20	67/120	58
Fe-MOF/g-C$_3$N$_4$	CR	Visible light (Xe)	40/100	25	87.1/120	59
g-C$_3$N$_4$/M-Fe-BTC	Reactive red 195	Sunlight	20/100	20	65/60	16
CdS/g-C$_3$N$_4$/Ti-MOF	RhB	Visible light (Xe)	10/50	10	90.2/90	60
Ni-MOF/g-C$_3$N$_4$ composite	RhB/CR	Sunlight	20/100	10	93/64/120	This work

Table 1. Comparison of photocatalytic dye degradation efficiency of different MOF/GCN composite reported in the literature and present study.

Fig. 9. (**a**) Mott–Schottky plots, (**b**) band edge positions, (**c**) scavenger studies, and (**d**) electrochemical impedance spectra of the various synthesized materials.

degradation efficiency was drastically decreased, indicating that the dye degradation process was largely driven by the superoxide radicals followed by hydroxyl radicals[56].

As one of the determining factors to manifest efficient photocatalytic reactions, the interfacial charge transfer efficiencies of the developed systems were analyzed by recording the electrochemical impedance spectra (EIS) of the samples, and the obtained Nyquist plots are given in Fig. 9d. From the obtained equivalent circuit (shown in the inset of Fig. 9d), the charge transfer resistance (R_{ct}) values of 426.8, 438.2, 551.3, 874.7, and 493.6 Ω were estimated for NTP, NATP, GCN, NTP/GCN, and NATP/GCN, respectively. The observed increased R_{ct} value for GCN can be attributed to its intrinsic electronic band structure, while the decreased R_{ct} values for NTP and NATP MOFs could be attributed to their electron-rich aromatic functional groups, efficiently promoting the electrons at the interface. Among the composites, the observed decreased resistance in NATP/GCN can be attributed to the presence of amino groups providing more electron-donating sites and increasing the overall electron density in the composite compared to NTP/GCN. As a result, these amino groups facilitate effective charge transfer processes and reduce charge transfer resistance at the interface. In addition, the band alignments between NATP and GCN are more favorable for the effective charge transfer in the NATP/GCN the system compared to NTP/GCN, greatly delocalizing electrons in the conduction band and facilitating electron transfer within the composites as well as at the interfaces[55,62].

Based on these observations from various characterizations and experiments conducted, a plausible photocatalytic mechanism of the developed NTP/GCN and NATP/GCN composites towards degradation of dye molecules can be proposed as follows. As illustrated in Fig. 10a, b, upon exciting the systems, both components of the composite absorb photons, generating electron–hole pairs. Upon excitation, the photogenerated electrons in the CB of NTP or NATP MOFs recombine with the holes in the VB of GCN. Meanwhile, the electrons in the CB of GCN and the holes in the VB of NTP or NATP remain separated. These spatially separated charge carriers then participate in the subsequent redox reactions. This enables the formation of a Z-scheme driven charge transfer mechanism in both the composites based on their band edge potentials illustrated in Fig. 9b. It is known that the Z-scheme facilitates the effective charge carrier separation in the systems, inhibiting the carrier recombination and improving the carrier lifetime in the photocatalysts. Accordingly, both the composites exhibited
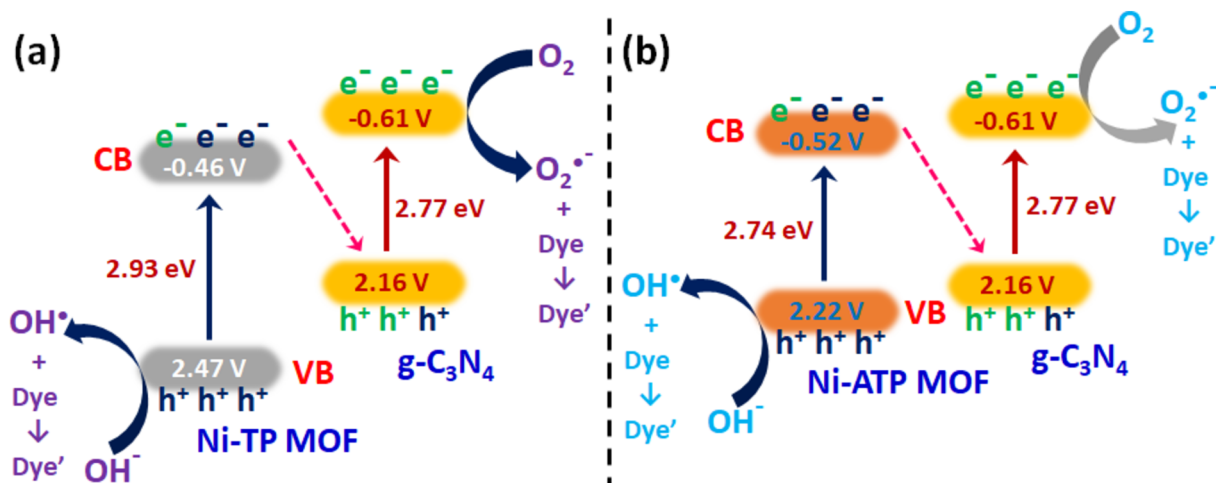
Fig. 10. Z-scheme driven photocatalytic degradation mechanism of (**a**) NTP/GCN and (**b**) NATP/GCN composite systems.

excellent photocatalytic properties due to their suitable band edge positions, meeting the required redox-potential facilitating the degradation of the dye molecules. It can be seen that the reduction reactions occur in the CB of the GCN, contributing to a consistent reductive degradation of the dye molecules in both systems. On the other hand, the oxidation reaction is largely driven by the VB of the respective MOFs, where the suitable oxidative potential of NATP MOF favors the effective dye-degradation compared to NTP MOFs[63].

However, as a composite system, the redox reactions collectively happen over both GCN and MOFs systems, and contributing to the overall photocatalytic degradation of dye molecules. It should be noted that the VB and CB of NATP MOFs align more favorably with GCN compared to NTP MOF. This ensures that the charge carrier transfer in NATP/GCN composite relatively rapid compared to the other system. From the band structure shown in Fig. 9b, it is clear that the NATP/GCN composite can effectively generate both the superoxide and hydroxyl radicals during the reaction. Conversely, even though the band structure of NTP/GCN composite is suitable for redox reactions, its VB potential is not suitable for the robust generation of hydroxyl radicals[64]. These observations provide further insights that the superoxide radicals, being weaker oxidants compared to hydroxyl radicals, are more selective in their reactions and may target specific functional groups or sites within the dye molecules, leading to more controlled and effective degradation. In addition, since the RhB and CR dyes contain electron-rich aromatic systems and side groups, they may react more readily with superoxide radicals, leading to efficient degradation. Similarly, superoxide radicals have a longer lifetime compared to hydroxyl radicals in aqueous solutions. This longer lifetime allows superoxide radicals to diffuse further from the photocatalyst surface, increasing the probability of encountering and reacting with dye molecules, thus enhancing the degradation process[54].
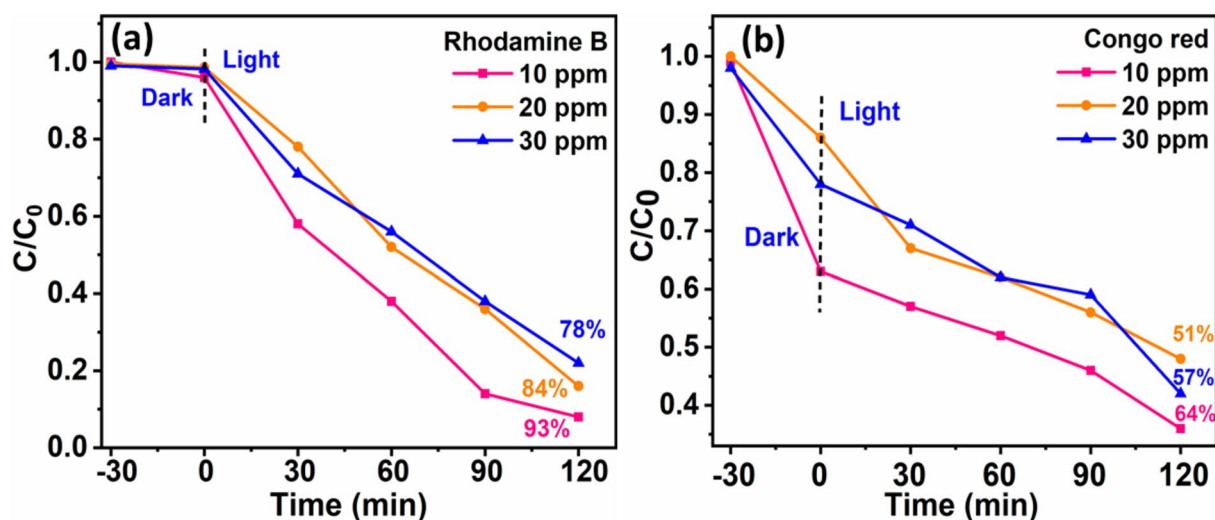
Effect of catalyst concentration

As the NATP/GCN composite exhibited enhanced photocatalytic activities, this system was further chosen for parametric studies. Accordingly, the catalyst concentration was varied to 10, 20, and 30 mg, while keeping the dye concentration at 10 ppm, dye-solution volume at 100 mL, and pH at ~7. The obtained results of catalyst concentration-dependent degradation of RhB and CR dyes are displayed in Fig. 11a, b, respectively. From the obtained C/C_0 ratio plots, it can be observed that in both cases, the degradation is found to be highest when the catalyst concentration was 20 mg (RhB ~93%, CR ~64% in 120 min). However, the degradation decreases when the catalyst concentration was increased to 30 mg (RhB ~71%, CR ~48% in 120 min). At higher concentrations (i.e., 30 mg), the excess amount of catalyst may agglomerate and inhibit the active sites in the system, leading to the suppression of radical generation during the photocatalytic reactions. This eventually leads to the decrement in the photocatalytic efficiency of the system[53].

Effect of dye concentration

Similar to varying the catalyst concentration, the concentrations of dyes (RhB and CR) were also varied to be 10, 20, and 30 pm, while keeping the catalyst concentration, solution volume, and pH at 20 mg, 100 mL, and 7, respectively. It can be observed from the obtained C/C_0 ratio plots shown in Fig. 12a, b that as the dye concentration was increased from 10 to 20 and 30 ppm, the degradation is found to be decreased from 93% to 84 and 78% for RhB and from 64% to 51 and 57% for CR. The observed decreased efficiency of the photocatalyst with increasing concentration of dye molecules can be attributed to the presence of insufficient radicals generated by the photocatalyst. Also, at higher concentrations, the dye-particle interaction and the distribution of dye molecules may be lesser compared to optimal conditions. Furthermore, the higher amount of dye molecules can also relatively hinder the interactions of light with photocatalyst through scattering of light scattering and reflectance effects, leading to the decreased efficiency in the degradation high-concentration dyes in the reaction solution[65].
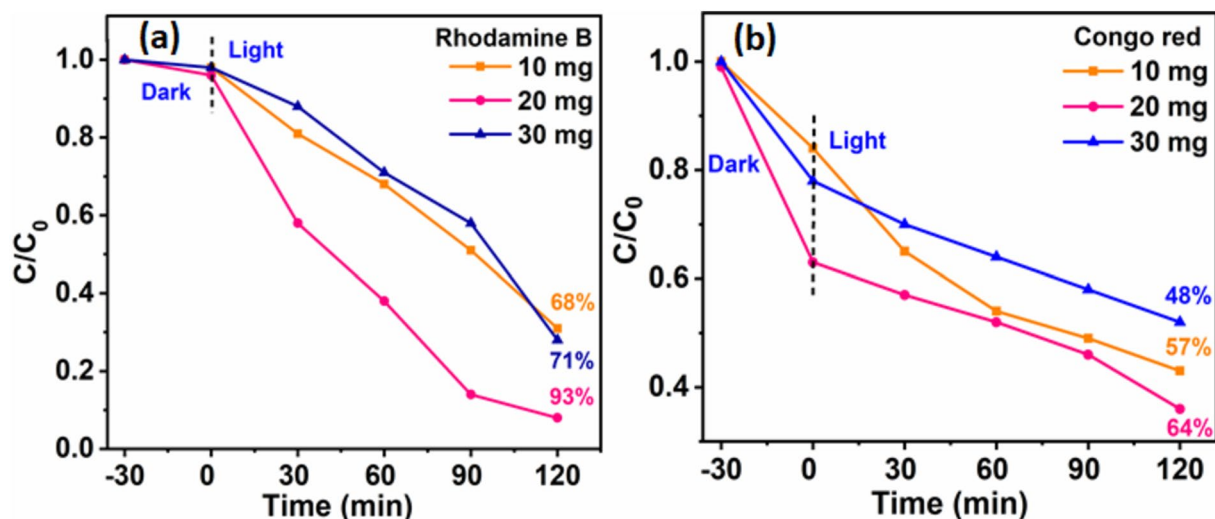
Fig. 11. Catalyst concentration dependent degradation of (**a**) rhodamine B and (**b**) Congo red dyes by NATP/GCN composite photocatalyst.
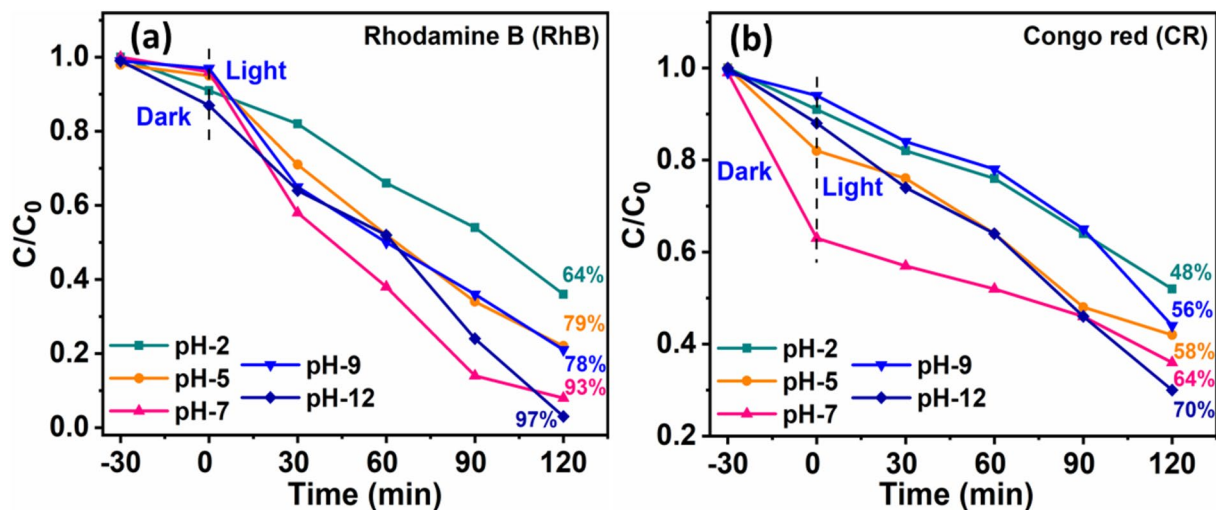

Fig. 12. Dye concentration dependent degradation of (**a**) rhodamine B and (**b**) Congo red dye by NATP/GCN composite photocatalyst.

Effect of pH

The pH of the solution can significantly alter the surface charge of the photocatalyst and dye molecules, leading to significantly influence the efficiency. The adsorption of dye molecules onto the catalyst surface, which is a crucial step in the photocatalytic degradation process, which is highly depends on the electrostatic interactions between the catalyst and the dye. Also, environmental and industrial applications of photocatalytic dye degradation may involve varying pH conditions. By understanding the pH dependence of degradation, the optimal conditions for favorable adsorption under specific environmental conditions can be determined, leading to improved degradation efficiency. Accordingly, pH of the dye solutions (RhB and CR) was varied to be ~ 2, 5, 7, 9, and 12 by keeping dye concentration to be 10 ppm of 100 mL solution and photocatalyst concentration (NATP/GCN) of 20 mg. The obtained results showed (Fig. 13a, b) that in lower (2, 5), neutral (7), and higher (9, 12) pH values, the degradation of RhB dye is around 64, 79, 93, 78, and 97%, respectively and it is around 48, 58, 64, 56, and 70% for CR dye respectively.

The observed decreased dye degradation at low pH values (i.e., pH 2 and 5) can be attributed to the protonation of both dye molecules and photocatalysts. Accordingly, in acidic medium, this protonation alters the electrostatic interactions and suppresses the active sites of the both MOFs and g-C$_3$N$_4$, leading to hinder the photocatalytic efficiency. Furthermore, it is also possible that the generation of reactive oxygen species like hydroxyl radicals can be suppressed under highly acidic conditions, leading to decreased overall photocatalytic activity[66].

Similarly, the observed decreased efficiency at basic pH values (i.e., pH 9) can be attributed to the alkaline nature of the reaction system leading to electrostatic imbalance between the catalyst and dye molecules, leading to decrease their interaction and thereby decrease the overall degradation of the dyes. In contrast, at higher pH

Fig. 13. pH-dependent photocatalytic degradation of (**a**) rhodamine B and (**b**) Congo red dye by NATP/GCN composite photocatalyst.

value (i.e., pH 12), an increment in dye degradation efficiency was observed could be attributed to the alkaline hydrolysis, rather than photocatalysis, which affects the stability and structural integrity of both MOF and g-C$_3$N$_4$ in the composite. The high concentration of hydroxide ions (OH$^-$) in alkaline solutions leads to modify the dye molecules, resulting in decolorization instead of degradation of the dye molecules[67].

Recyclability test

The recyclability of the NATP/GCN composite photocatalyst was investigated for the degradation of RhB and CR dyes, and the obtained C/C$_0$ plots are presented in Fig. 14a, b, respectively.

The recycling studies were carried out with 10 ppm of RhB and CR dyes, and 20 mg of the NATP/GCN composite was stirred in the dark for 30 min to attain adsorption–desorption equilibrium, then exposed to sunlight and gently stirred to maintain dispersion during the reaction. Notably, adsorption during recycling was also observed, and it declined with each cycle. However, this adsorption data has not been provided in the plots to emphasize only the cyclic photocatalytic degradation efficiency of the developed photocatalyst, as shown in Fig. 14a, b. The results show that the cyclic degradation efficiency of the NATP/GCN composite is consistent for up to 5 cycles with ~ 88% degradation efficiency for RhB. However, for CR, the degradation remains stable for up to 4 cycles with a around 70% degradation efficiency and in 5th cycle, the efficiency was decreased to around 56%. Overall, the obtained results suggest that the NATP/GCN composite could be effective for the degradation of both cationic (RhB) and anionic dyes (CR), which can be attributed to the synergistic properties of both GCN and NATP MOF, making it an optimal photocatalytic system for dye-degradation applications.

Further, the structural, morphological, and optical stability of the recycled NATP/GCN composite system employed to degrade RhB dye was analyzed by obtaining its XRD pattern, FESEM, and UV–visible absorption
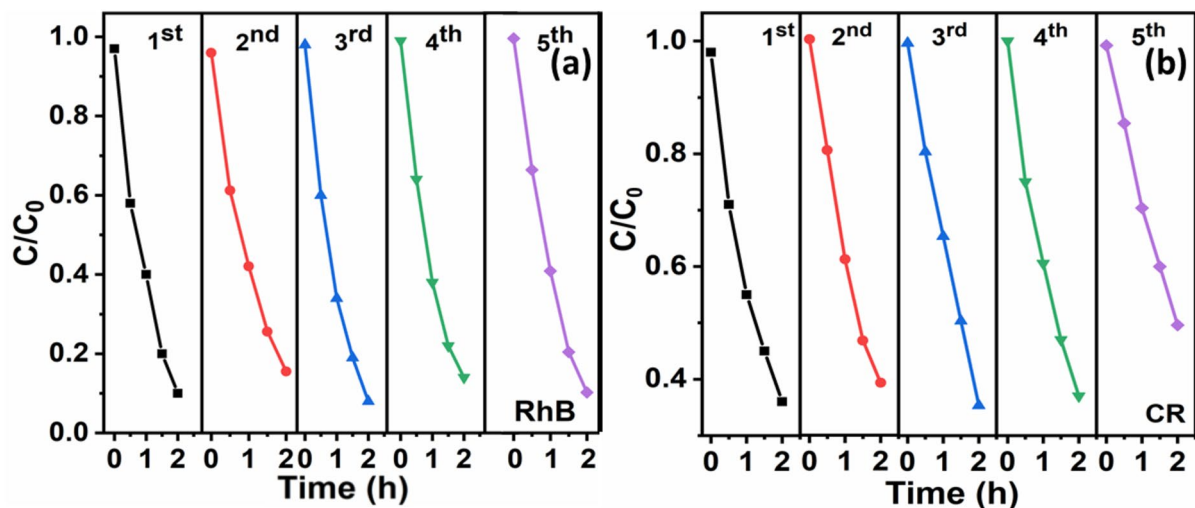

Fig. 14. Recycle efficiency of NATP/GCN composite towards degradation of (**a**) rhodamine B and (**b**) Congo red dyes.

spectra, and Tauc's plots after the cyclic dye degradation studies (5th cycle). The obtained results are displayed in Fig. 15a–d, respectively, and the photographs of the fresh and recycled NATP/GCN composite system are given in the inset of Fig. 15a. From the observed consistent features in the XRD pattern, FESEM image, absorption spectra, and band gap energy of the recycled photocatalyst with that of the fresh photocatalyst, it can be corroborated that the crystal structure, surface morphology, and optical property of the composites are hardly altered, suggesting the enhanced structural and physiochemical stability of the developed NATP/GCN composite system. The cyclic ability of the photocatalyst enhances cost-effectiveness by reducing the need for frequent replacements, which lowers operational expenses and makes the process more economically viable. Further, it supports sustainability by minimizing waste and extending the lifecycle of materials, aligning with green chemistry principles and reducing environmental impact. Consistent photocatalytic activity across multiple cycles ensures reliable performance, which is crucial for industrial and large-scale applications that require dependable results for effective pollutant degradation.

Conclusion

In this study, nickel-based metal–organic frameworks (Ni-MOFs) constructed with the 2-amino terephthalic acid ligand (NATP) exhibited superior physicochemical properties compared to those developed with the terephthalic acid ligand (NTP). The incorporation of these Ni-MOFs into composites with g-C_3N_4 (GCN) further enhanced their properties due to the synergistic interactions between the components. The structural and morphological analyses of the formed materials, conducted using XRD and FESEM techniques, suggested that the NATP/GCN composite exhibited a stable composite system formation, which is considered a pathway mechanism. Consequently, the NATP/GCN composite exhibited remarkable photocatalytic performance, degrading ~ 93% of rhodamine B (RhB) within 120 min under solar light irradiation. However, it showed relatively lower efficiency for the anionic Congo red (CR) dye, degrading about 64% in 120 min. Nevertheless, NATP/GCN consistently outperformed the NTP/GCN composite. This superior performance can be attributed to the ligand-induced positioning of the valence and conduction band edges at suitable potentials, enabling the generation of highly active $O_2^{\cdot-}$ radical species followed by OH· radicals. These radicals facilitated effective redox-mediated degradation of
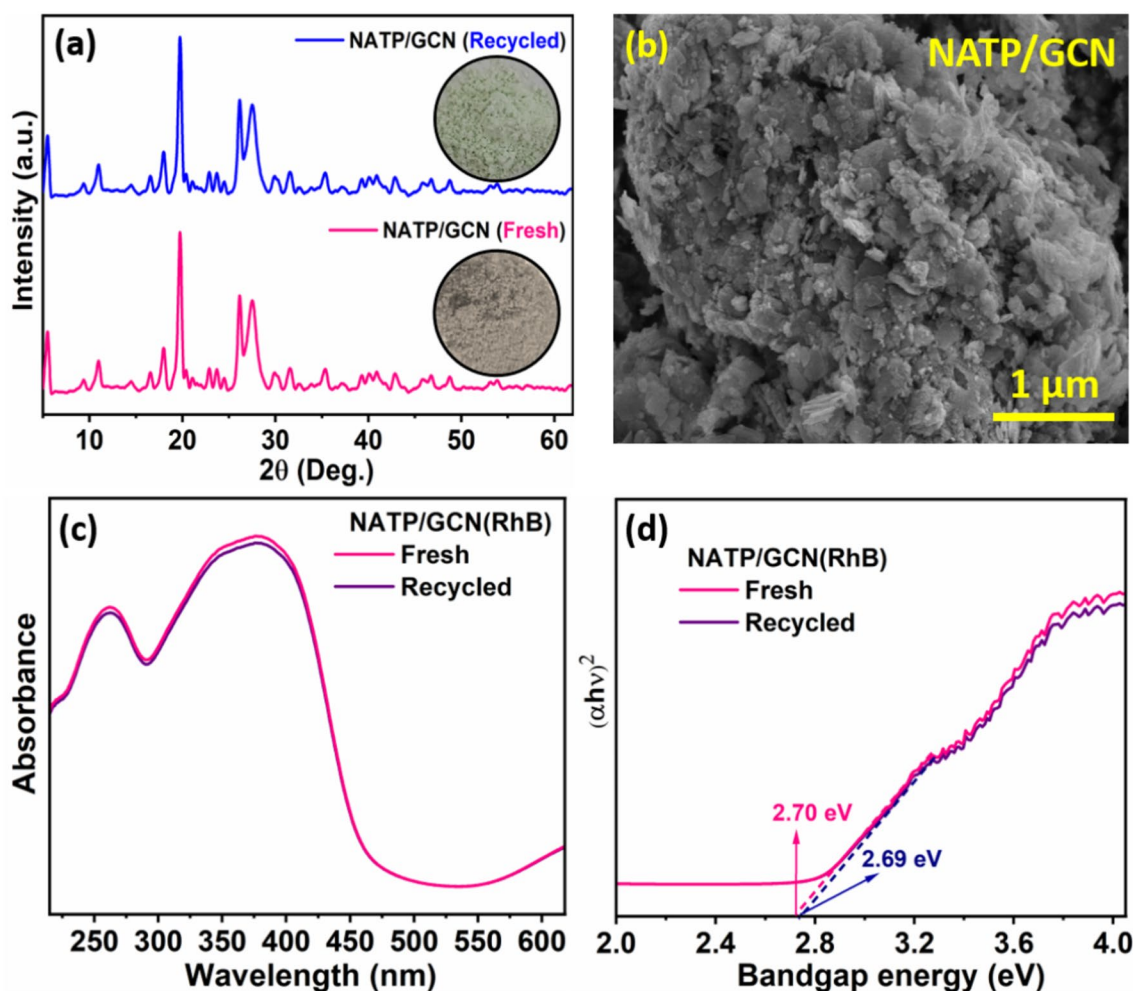
Fig. 15. (**a**) XRD pattern, (**b**) FESEM image, (**c**) UV–Visible absorption spectra, and (**d**) Tauc's plot for bandgap estimation of the fresh and 5th recycled NATP/GCN photocatalyst (Insert of (**a**): photographic image of the fresh and recycled photocatalyst).

both cationic (rhodamine B) and anionic (Congo red) dyes under solar light irradiation. The enhanced activity of NATP/GCN is likely due to the improved charge separation, increased light absorption, and more favorable band alignment for redox reactions driven by the Z-scheme mechanism. The physicochemical investigations and parametric studies conducted suggest that the NATP/GCN composite can be explored for its ligand-dependent features and synergetic effects, through which its properties can be suitably modified for desired applications. In addition, the stability and reusability of the NATP/GCN composite under prolonged use has also been assessed to determine its viability for large-scale applications.

Data availability

Data is provided within the manuscript.

References
1. Al-Tohamy, R. *et al.* A critical review on the treatment of dye-containing wastewater: Ecotoxicological and health concerns of textile dyes and possible remediation approaches for environmental safety. *Ecotoxicol. Environ. Saf.* **231**, 113160 (2022).
2. Umar, M., Roddick, F. & Fan, L. Recent advancements in the treatment of municipal wastewater reverse osmosis concentrate-an overview. *Crit. Rev. Environ. Sci. Technol.* **45**, 193–248 (2015).
3. Rajasulochana, P. & Preethy, V. Comparison on efficiency of various techniques in treatment of waste and sewage water–a comprehensive review. *Resource-Effic. Technol.* **2**, 175–184 (2016).
4. Pavel, M. *et al.* Photocatalytic degradation of organic and inorganic pollutants to harmless end products: Assessment of practical application potential for water and air cleaning. *Catalysts.* **13**, 380 (2023).
5. Etacheri, V., Di Valentin, C., Schneider, J., Bahnemann, D. & Pillai, S. C. Visible-light activation of TiO_2 photocatalysts: Advances in theory and experiments. *J. Photochem. Photobiol. C Photochem. Rev.* **25**, 1–29 (2015).
6. Li, Z., Meng, X. & Zhang, Z. Recent development on MoS_2-based photocatalysis: A review. *J. Photochem. Photobiol. C Photochem. Rev.* **35**, 39–55 (2018).
7. Ren, G. *et al.* Recent advances of photocatalytic application in water treatment: A review. *Nanomaterials.* **11**, 1804 (2021).
8. Balu, S., Ganapathy, D., Arya, S., Atchudan, R. & Sundramoorthy, A. K. Advanced photocatalytic materials-based degradation of micropollutants and their use in hydrogen production a review. *RSC Adv.* **14**, 14392–14424 (2024).
9. Lee, D. E., Kim, M. K., Danish, M. & Jo, W. K. State-of-the-art review on photocatalysis for efficient wastewater treatment: Attractive approach in photocatalyst design and parameters affecting the photocatalytic degradation. *Catal. Commun.* **183**, 106764 (2023).
10. Yusuf, V. F., Malek, N. I. & Kailasa, S. K. Review on metal–organic framework classification, synthetic approaches, and influencing factors: Applications in energy, drug delivery, and wastewater treatment. *ACS Omega* **7**, 44507–44531 (2022).
11. Özcan, E., Mermer, Z. & Zorlu, Y. Metal-organic frameworks as photocatalysts in energetic and environmental applications. *Turk. J. Chem.* **47**, 1018–1052 (2023).
12. Yuan, L. *et al.* Metal-organic framework-based S-scheme heterojunction photocatalysts. *Nanoscale* **16**, 5487–5503 (2024).
13. Matias, M. L. *et al.* Microwave synthesis of visible-light-activated g-C_3N_4/TiO_2 photocatalysts. *Nanomaterials.* **13**, 1090 (2023).
14. Wudil, Y. *et al.* Tuning of graphitic carbon nitride (g-C_3N_4) for photocatalysis: A critical review. *Arab. J. Chem.* **16**, 104542 (2023).
15. Li, X. *et al.* Facilitation of the visible light-induced Fenton-like excitation of H_2O_2 via heterojunction of g-C_3N_4/NH_2-Iron terephthalate metal-organic framework for MB degradation. *Appl. Catal. B.* **202**, 653–663 (2017).
16. Huang, W., Liu, N., Zhang, X., Wu, M. & Tang, L. Metal organic framework g-C_3N_4/MIL-53(Fe) heterojunctions with enhanced photocatalytic activity for Cr(VI) reduction under visible light. *Appl. Surf. Sci.* **425**, 107–116 (2017).
17. Ren, J. *et al.* Construction of efficient g-C_3N_4/NH_2-UiO-66 (Zr) heterojunction photocatalysts for wastewater purification. *Sep. Purif. Technol.* **274**, 118973 (2021).
18. Cao, Y., Chen, X., Li, X. & Wang, B. Tuning surface functionalization and pore structure of UiO-66 metal–organic framework nanoparticles for organic pollutant elimination. *ACS Appl. Nano Mater.* **4**, 5486–5495 (2021).
19. Gayathri, K. *et al.* In situ-grown ZnO particles on g-C_3N_4 layers: A direct Z-scheme-driven photocatalyst for the degradation of dye and pharmaceutical pollutants under solar irradiation. *J. Mater. Sci. Mater. Electron.* **33**, 9774–9784 (2022).
20. Xu, T., Hou, X., Liu, S. & Liu, B. One-step synthesis of magnetic and porous Ni@ MOF-74 (Ni) composite. *Microporous Mesoporous Mater.* **259**, 178–183 (2018).
21. Yan, Y. *et al.* Facile synthesis of an accordion-like Ni-MOF superstructure for high-performance flexible supercapacitors. *J. Mater. Chem. A.* **4**, 19078–19085 (2016).
22. Gao, S. *et al.* Facile synthesis of cuboid Ni-MOF for high-performance supercapacitors. *J. Mater. Sci.* **53**, 6807–6818 (2018).
23. Durmus, Z. *et al.* Preparation and characterization of Ce-MOF/g-C_3N_4 composites and evaluation of their photocatalytic performance. *Ceram. Int.* **49**, 24428–24441 (2023).
24. Zhou, W. J. *et al.* Synthesis of a 3D Cu (II) MOF and its heterostructual g-C_3N_4 composite showing improved visible-light-driven photodegradation of organic dyes. *J. Solid State Chem.* **315**, 123520 (2022).
25. Ravikumar, M. P. *et al.* Insights into the photocatalytic memory effect of magneto-plasmonic Ag–Fe_3O_4@ TiO_2 ternary nanocomposites for dye degradation and H_2 production under light and dark conditions. *Energy Fuels.* **36**, 11503–11514 (2022).
26. Prakash, R. M. *et al.* One-step solution auto-combustion process for the rapid synthesis of crystalline phase iron oxide nanoparticles with improved magnetic and photocatalytic properties. *Adv. Powder Technol.* **33**, 103435 (2022).
27. Radhika, M. *et al.* Electrochemical studies on Ni, Co & Ni/Co-MOFs for high-performance hybrid supercapacitors. *Mater. Res. Express.* **7**, 054003 (2020).
28. Karthik, G., Vinothkumar, K., Mohan, S. & Balakrishna, R. G. Synergy of ligands in tailoring the photocatalytic properties of zirconium metal–organic framework-impregnated membranes for water treatment. *Ind. Eng. Chem. Res.* **63**, 6743–6753 (2024).
29. Shi, C. *et al.* Nickel metal-organic framework nanoparticles as electrode materials for Li-ion batteries and supercapacitors. *J. Solid State Chem.* **21**, 2415–2423 (2021).
30. Roshni, C. P., Jithesh, K., Manuraj, M., Raj, K. G. & Rakhi, R. B. β-Ni $(OH)_2$ supported over g-C_3N_4: A novel catalyst for para-nitrophenol reduction and supercapacitor electrode. *Results Chem.* **4**, 100498 (2022).
31. Vinothkumar, K., Kanagaraj, V., Padaki, M. & Balakrishna, R. G. Tannic Acid-functionalized MoS_2 and g-C_3N_4 thin film lamellar membranes for improved permeance and rejection in nanofiltration. *ACS Appl. Nano Mater.* **9**, 10396–10407 (2024).
32. Gao, Y. *et al.* A photo-Fenton self-cleaning membrane based on NH_2-MIL-88B (Fe) and graphene oxide to improve dye removal performance. *J. Membr. Sci.* **626**, 119192 (2021).
33. Gayathri, K. *et al.* Ligand-mediated band structure engineering and physiochemical properties of UiO-66 (Zr) metal-organic frameworks (MOFs) for solar-driven degradation of dye molecules. *Colloids Surf. A Physicochem. Eng. Asp.* **653**, 129992 (2022).
34. Vinothkumar, K. & Balakrishna, R. G. One-pot synthesis of NH_2-MIL-101 (Fe) and α–Fe_2O_3 composite as efficient heterojunction for multifunctional photocatalytic membranes: Towards zero waste generation. *Appl. Catal. B.* **340**, 123199 (2024).

35. Dong, F., Li, Y., Wang, Z. & Ho, W. K. Enhanced visible light photocatalytic activity and oxidation ability of porous graphene-like g-C$_3$N$_4$ nanosheets via thermal exfoliation. *Appl. Surf. Sci.* **358**, 393–403 (2015).

36. Liu, X. *et al.* Crystal transformation of metal–organic frameworks to boost visible-light photocatalysis via amine adsorption. *J. Mater. Chem.* **12**, 2200–2208 (2024).

37. Zhao, F. *et al.* MIL-101 (Fe)/g-C$_3$N$_4$ for enhanced visible-light-driven photocatalysis toward simultaneous reduction of Cr (VI) and oxidation of bisphenol A in aqueous media. *Appl. Catal. B.* **272**, 119033 (2020).

38. Giannakoudakis, D. A., Travlou, N. A., Secor, J. & Bandosz, T. J. Oxidized g-C$_3$N$_4$ nanospheres as catalytically photoactive linkers in MOF/g-C$_3$N$_4$ composite of hierarchical pore structure. *Small* **13**, 1601758 (2017).

39. Mazlan, N. A. *et al.* The growth of metal–organic frameworks in the presence of graphene oxide: A mini review. *Membranes.* **12**, 501 (2022).

40. Soni, A., Sharma, R., Rana, D. S., Singh, D. & Gupta, N. Structural designs of functional metal organic frameworks for the detection of mercury in contaminated water sources. *Coord. Chem. Rev.* **494**, 215343 (2023).

41. Wang, K. *et al.* Rational design of recyclable metal-organic frameworks-based materials for water purification: An opportunity for practical application. *Sci. Total Environ.* **12**, 164345 (2023).

42. Pullen, S. & Clever, G. H. Mixed-ligand metal–organic frameworks and heteroleptic coordination cages as multifunctional scaffolds a comparison. *Acc. Chem. Res.* **51**, 3052–3064 (2018).

43. Chandra, L., Vinothkumar, K. & Balakrishna, R. G. MIL-100 (Fe) integrated fibrous polyvinyl alcohol graft on cellulose acetate towards the development of green membranes; Application in multi solute rejection. *J. Environ. Chem. Eng.* **11**, 109851 (2023).

44. Feng, X., Long, R., Liu, C. & Liu, X. Novel dual-heterojunction photocatalytic membrane reactor based on Ag$_2$S/NH$_2$-MIL-88B (Fe)/poly (aryl ether nitrile) composite with enhanced photocatalytic performance for wastewater purification. *J. Chem. Eng.* **454**, 139765 (2023).

45. Ravikumar, M. P. *et al.* Observation of inherited plasmonic properties of TiN in titanium oxynitride (TiOxNy) for solar-drive photocatalytic applications. *Environ. Res.* **229**, 115961 (2023).

46. Tan, Q. *et al.* Magnetically induced construction of core–shell architecture Fe$_3$O$_4$@ TiO$_2$–Co nanocomposites for effective photocatalytic degradation of tetracycline. *New J. Chem.* **47**, 15951–15962 (2023).

47. Amini, A., Karimi, M., Rabbani, M. & Safarifard, V. Cobalt-doped g-C$_3$N$_4$/MOF heterojunction composite with tunable band structures for photocatalysis aerobic oxidation of benzyl alcohol. *Polyhedron* **216**, 115728 (2022).

48. Pattappan, D., Vargheese, S., Kavya, K. V., Kumar, R. R. & Haldorai, Y. Metal-organic frameworks with different oxidation states of metal nodes and aminoterephthalic acid ligand for degradation of Rhodamine B under solar light. *Chemosphere* **286**, 131726 (2022).

49. Ye, R. *et al.* Fabrication of CoTiO$_3$/g-C$_3$N$_4$ hybrid photocatalysts with enhanced H$_2$ evolution: Z-scheme photocatalytic mechanism insight. *ACS Appl. Mater. Interfaces.* **8**, 13879–13889 (2016).

50. Althabaiti, S. A. *et al.* PtOx deposited Fe$_3$O$_4$-ZnO/TiO$_2$ nanocomposites for photocatalytic H$_2$ production under visible light. *J. Environ. Chem. Eng.* **11**, 110615 (2023).

51. Rasilingwani, T., Gumbo, J., Masindi, V. & Foteinis, S. Removal of Congo red dye from industrial effluents using metal oxide-clay nanocomposites: Insight into adsorption and precipitation mechanisms. *Water Resour.* **31**, 100253 (2024).

52. Durmus, Z. *et al.* Preparation and characterization of Ce-MOF/g-C$_3$N$_4$ composites and evaluation of their photocatalytic performance. *Ceram. Int.* **49**, 24428–24441 (2023).

53. Kumaravel, S. *et al.* Rational construction of MOF derived α-Fe$_2$O$_3$/g-C$_3$N$_4$ composite for effective photocatalytic degradation of organic pollutants and electrocatalytic oxygen evolution reaction. *Spectrochim. Acta Part A Mol. Biomol. Spectrosc.* **310**, 123972 (2024).

54. Pan, Y. *et al.* Fabrication of MIL-Fe (53)/modified g-C$_3$N$_4$ photocatalyst synergy H$_2$O$_2$ for degradation of tetracycline. *Sep. Purif. Technol.* **279**, 119661 (2021).

55. Ma, S., Xia, X., Song, Q., Zhao, Y. & Yang, J. Heterogeneous junction Ni-MOF@ BiOBr composites: Photocatalytic degradation of methylene blue and ciprofloxacin. *Solid State Sci.* **138**, 107135 (2023).

56. Devarayapalli, K. C., Prabhakar Vattikuti, S. V., Sreekanth, T. V., Nagajyothi, P. & Jaesool, S. Facile synthesis of Ni-MOF using microwave irradiation method and application in the photocatalytic degradation. *Mater. Res. Express.* **6**, 11 (2019).

57. Zhang, L. *et al.* Photocatalytic hydrogen evolution and tetracycline degradation over a novel Z-scheme Ni-MOF/g-C$_3$N$_4$ heterojunction. *Colloids Surf. A Physicochem. Eng. Asp.* **686**, 133297 (2024).

58. Sedaghati, N., Habibi-Yangjeh, A. & Khataee, A. Fabrication of g-C$_3$N$_4$ nanosheet/Bi$_5$O$_7$Br/NH$_2$-MIL-88B (Fe) nanocomposites: Double S-scheme photocatalysts with impressive performance for the removal of antibiotics under visible light. *Int. J. Miner. Metall. Mater.* **30**, 1363–1374 (2023).

59. Rana, G. *et al.* Visible-light driven Z-scheme g-C$_3$N$_4$/Fe-MOF photocatalyst for degradation of organic pollutants. *J. Inorg. Organomet. Polym.* **34**, 2688–2704 (2024).

60. Ying, C., Boyin, Z., Yuning, L., Yongchao, L. & Jing, L. Preparation of CdS/g-C$_3$N$_4$/MOF composite with enhanced visible-light photocatalytic activity for dye degradation. *J. Solid State Chem.* **274**, 32–39 (2023).

61. Pattappan, D. *et al.* Visible light photocatalytic activity of a FeCo metal-organic framework for degradation of acetaminophen and 2, 4-dichlorophenoxyacetic acid and a nematode-based ecological assessment. *J. Chem. Eng.* **464**, 142676 (2023).

62. Jayaraj, S. K. & Thangadurai, P. Surface decorated V$_2$O$_5$ nanorods with Pt nanoparticles for enriched visible light photocatalytic performance for the photodegradation of Rh-6G. *J. Mol. Liq.* **319**, 114368 (2020).

63. Jayaraj, S. K. & Paramasivam, T. Surface engineering of Au decorated V$_2$O$_5$ nanorods enhanced photodegradation of Rh-6G under visible light with high cyclability and stability. *J. Environ. Chem. Eng.* **7**, 103512 (2019).

64. Konstas, P. S., Konstantinou, I., Petrakis, D. & Albanis, T. Synthesis, characterization of g-C$_3$N$_4$/SrTiO$_3$ heterojunctions and photocatalytic activity for organic pollutants degradation. *Catalysts* **8**, 554 (2018).

65. Zhang, N. *et al.* Moisture stable Ni-Zn MOF/g-C$_3$N$_4$ nanoflowers: A highly efficient adsorbent for solid-phase microextraction of PAHs. *J. Chromatogr. A.* **1556**, 37–46 (2018).

66. Li, H., Gong, H. & Jin, Z. Phosphorus modified Ni-MOF–74/BiVO$_4$ S-scheme heterojunction for enhanced photocatalytic hydrogen evolution. *Appl. Catal. B.* **307**, 121166 (2022).

67. Ramos, V. M. *et al.* Degradation of diclofenac in water under LED irradiation using combined g-C$_3$N$_4$/NH$_2$-MIL-125 photocatalysts. *J. Hazard. Mater.* **416**, 126199 (2021).

Acknowledgements

Author contributions

G.K. conducted the experiments, collected the data, and wrote the main manuscript text; S.M. and R.G.B. made initial idea, designed the concept, validated the results, head of the project, and edited the manuscript text.

Competing interests

The authors declare no competing interests.

Additional information

Correspondence and requests for materials should be addressed to S.M. or R.G.B.

Reprints and permissions information is available at www.nature.com/reprints.

Publisher's note Springer Nature remains neutral with regard to jurisdictional claims in published maps and institutional affiliations.